catalysts

MDPI

Article

Waste-Extracted Zn and Ag Co-Doped Spent Catalyst-Extracted V_2O_5 for Photocatalytic Degradation of Congo Red Dye: Effect of Metal-Nonmetal Co-Doping

Nasser H. Shalaby [1,*], Saedah R. Al-Mhyawi [2], Ahmed H. Ragab [3], H. A. Elmawgoud [1], Eman A. Al-Swat [4] and Noha M. Al-Thubaiti [5]

[1] Egyptian Petroleum Research Institute, 1 Ahmed El-Zomor St., Cairo 11727, Egypt
[2] Department of Chemistry, College of Science, University of Jeddah, Jeddah 21419, Saudi Arabia
[3] Chemistry Department, Faculty of Science, King Khalid University, P.O. Box 9004, Abha 61413, Saudi Arabia
[4] Chemistry Department, College of Science, Umm Al-Qura University, Makkah 21955, Saudi Arabia
[5] Chemistry Department, College of Science, Prince Sattam Bin Abdulaziz University, Alkharj 11942, Saudi Arabia
* Correspondence: chem.shalaby@gmail.com; Tel.: +20-227-45-902

Abstract: The current study applies the eco-friendly principle of "wastes treat wastes". By swift methods, a composite photocatalyst was prepared from waste-extracted oxides, namely V_2O_5, Ag, and ZnO. The metal–lixiviant complexes were used as metal precursors, where the lixiviants act as auto-templates and increase the compatibility between the mixed metallic species, and their controlled thermal removal generates pores. The tri-constitute composite catalyst was doped with nitrogen. The constitution, surface composition, and optical properties of the doped catalysts were investigated by XRD, SEM, TEM, BET surface analysis, XPS, diffuse reflectance, and PL spectra. The as-prepared catalysts were employed in the photodegradation of Congo red dye (CR) under visible irradiation at ambient temperature. The degree of Ag dispersion had a significant effect on the bandgap, as did metal and metal-nonmetal co-doping. The efficiency of dye removal changes dramatically with time up to 120 min, after which it begins to decrease. According to the pH effect, the normal pH of Congo red dye (6.12) is optimal. At a catalyst dose of 1 g L^{-1} and an irradiation period of 120 min, photodegradation efficiency reached 89.9% and 83.4% over [$Ag_{0.05}$ $ZnO_{0.05}$ $V_2O_{5(0.90)}$] and [$Ag_{0.05}$ $ZnO_{0.05}$ $V_2O_{5(0.90)}$]$_N$, respectively. The kinetic study depicted the significant role of mass transfer in the reaction rate. The obtained rate constants were 0.995 mole L^{-1} S^{-1} and 0.998 mole L^{-1} S^{-1} for [$Ag_{0.05}$ $ZnO_{0.05}$ $V_2O_{5(0.90)}$] and [$Ag_{0.05}$ $ZnO_{0.05}$ $V_2O_{5(0.90)}$]$_N$, respectively.

Keywords: waste-extracted Zn and Ag; spent catalyst-extracted V_2O_5; auto-templated; metal-nonmetal co-doping

check for updates

Citation: Shalaby, N.H.; Al-Mhyawi, S.R.; Ragab, A.H.; Elmawgoud, H.A.; Al-Swat, E.A.; Al-Thubaiti, N.M. Waste-Extracted Zn and Ag Co-Doped Spent Catalyst-Extracted V_2O_5 for Photocatalytic Degradation of Congo Red Dye: Effect of Metal-Nonmetal Co-Doping. *Catalysts* **2023**, *13*, 584. https://doi.org/10.3390/catal13030584

Academic Editor: Ioannis Konstantinou

Received: 5 February 2023
Revised: 3 March 2023
Accepted: 8 March 2023
Published: 14 March 2023

Copyright: © 2023 by the authors. Licensee MDPI, Basel, Switzerland. This article is an open access article distributed under the terms and conditions of the Creative Commons Attribution (CC BY) license (https://creativecommons.org/licenses/by/4.0/).

1. Introduction

The urgent demand for eco-friendly materials and chemical technologies has received a lot of attention due to environmental contamination and the scarcity of natural energy resources. Photocatalysis is one of the most promising solutions for not only dealing with environmental contaminants, but also harnessing solar energy as an alternative natural resource due to the depletion of conventional energy sources [1]. Wastewater treatment has become a pressing issue due to the increase in world population and industrial development. It is well known that the textile industry's waste waters include significant levels of non-fixed dyes, particularly azo dyes [2]. Some azo dyes and their byproducts, including aromatic amines, are well known to be very carcinogenic [3]. According to the data, approximately 10,000 metric tons of dyes are generated annually. Because dyeing wastewater is highly harmful to the environment, people are becoming more and more concerned about it [4]. The colored water shields the sunlight to penetrate the stream, which affects the

aquatic life [5]. The textile industry makes substantial use of CR among dyes. The primary reason Congo red cannot be decolored effectively is that it is designed to withstand fading, which causes biological destruction [6]. The most common techniques for removing textile dyes from wastewater include a variety of physical, chemical, and biological procedures such as adsorption onto activated carbon, coagulation, flocculation, chlorination, ozonization, biodegradation, and others. The fundamental disadvantage of these techniques is the development of a pollutant-containing phase that is more concentrated [5,7]. Recent advances in the chemical treatment of wastewater involve the oxidative degradation of organic contaminants dissolved in water. To overcome these challenges, heterogeneous photocatalysis using semiconductor materials has emerged as the most effective and eco-friendly advanced oxidation process for the removal of textile dyes from wastewater [8,9]. On the other hand, the large bandgap of a photocatalyst limits the photoabsorption to only the UV region of the solar spectrum, which accounts for approximately 4% of solar energy [10]. Therefore, it is crucial to design, create, and modify the physicochemical and optical properties in order to utilize the most of a significant portion of the solar spectrum. In fact, several research papers have been published on the doping of transition metals to engineer their electrical and photocatalytic capabilities in photodegradation of organic pollutants [9,11–14]. Vanadium pentoxide is an oxyanion of vanadium with a bandgap of 2.3 eV [15]. The photocatalytic activity of V_2O_5 in powder form stimulates it as a viable prospect for the degradation of various organic molecules [16]. However, the vanadium alkoxides used as vanadium precursors are very expensive.

The current study aims to prepare cheap and eco-friendly composite catalyst using waste-extracted metals oxide, namely V_2O_5 from spent catalyst, ZnO from blast furnace and Ag from silver solution waste. The hybridization of spent catalyst-extracted vanadia with ZnO and Ag engineers the bandgap energy and enhances the visible light absorption to harvest a significant portion of the visible light and utilize the metallic species synergism. Due to the surface plasmon resonance of Ag, it enhances the harvesting of visible light while the metal–semiconductor interface efficiently separates the photogenerated electrons and holes [17]. In addition, metal-nonmetal doping was discussed.

2. Results

The current research work focuses on two environmental perspectives in the application of the principle "wastes treat wastes". One concerns the reuse of wastewater, while the other explores the utilization of solid waste containing different chemicals resulting from different applications that are harmful if not used. This research focuses on the development of hybrid photocatalytic systems based on mixed oxides using spent catalyst, blast furnace slag, and photographic process waste as a worthless source of hybrid oxides. During the preparation of the hybrid photocatalyst, the ammonium salt and the organic salt of metal precursors were used to act as an auto-template for pores generation and to enhance the "histocompatibility" between the different mixed components. The as-prepared photocatalysts were evaluated for the removal of Congo red dye from wastewater.

2.1. Description of Structure

Figure 1 illustrates the IR spectra of the as-prepared catalysts. It is observed that the spectrum of [$Ag_{0.05}$ $ZnO_{0.05}$ $V_2O_{5(0.90)}$] is markedly different from those of [$Ag_{0.05}$ $ZnO_{0.05}$ $V_2O_{5(0.90)}]_N$ due to the restructuring of the surface network as a result of the formation of metal nitrides of Zn and V, which is in good agreement with other analyses (cf. XRD and XPS). The different characteristic peaks are assigned as depicted in Figure 1 [18–20].

The XRD patterns of [$Ag_{0.05}$ $ZnO_{0\cdot05}$ $V_2O_{5(0.90)}$] and [$Ag_{0.05}$ $ZnO_{0.05}$ $V_2O_{5(0.90)}]_N$ have been interpreted using JCPDS No. 89-2483, ICDD PDF No. 35-768, and ICSD No. 98-018-0878, Figure 2. The XRD profile of [$Ag_{0.05}$ $ZnO_{0.05}$ $V_2O_{5(0.90)}$] illustrates nanocrystals of V_2O_5 and zinc vanadate with different planes and a high degree of crystallinity, while the Ag nanoparticles exhibit a low degree of crystallinity. A small peak is observed at $2\theta = 38.2°$, which is characteristic of metallic Ag [21]. The absence of diffraction peaks by virtue of

silver doping shows that dopant silver is repelled on the crystal surface (cf. Figure 5) [22]. It is obvious that doping with nitrogen collapsed the crystal structure due to the formation of metal nitrides.

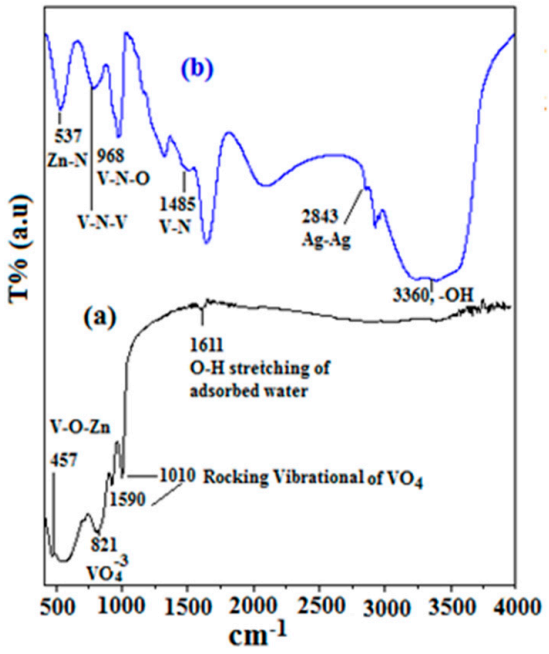

Figure 1. IR spectra of (**a**) [$Ag_{0.05}$ $ZnO_{0.05}$ $V_2O_{5(0.90)}$]; and (**b**) [$Ag_{0.05}$ $ZnO_{0.05}$ $V_2O_{5(0.90)}$]$_N$.

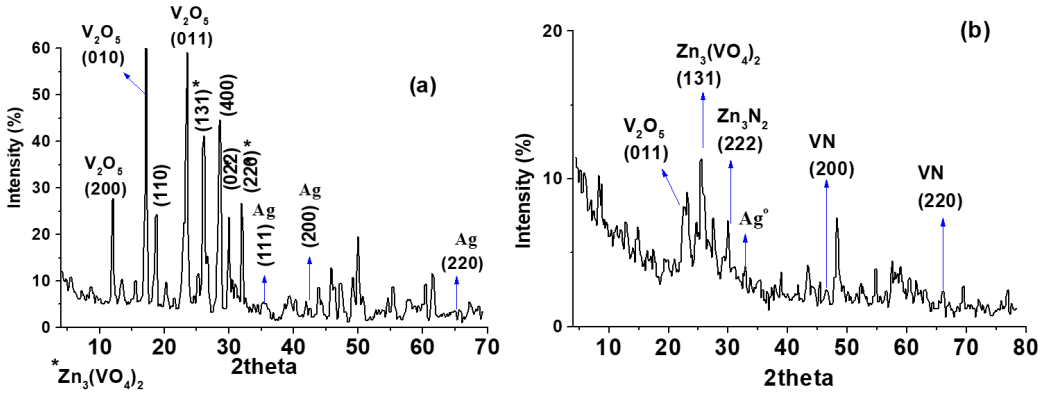

Figure 2. The XRD patterns of: (**a**) [$Ag_{0.05}$ $ZnO_{0.05}$ $V_2O_{5(0.90)}$]; and (**b**) [$Ag_{0.05}$ $ZnO_{0.05}$ $V_2O_{5(0.90)}$]$_N$.

The surface chemistry and the oxidation states of the metallic species were investigated by XP-spectra. Figure 3 depicts the survey spectrum and the deconvolution spectra of V, Zn, Ag, and O on the surface of [$Ag_{0.05}$ $ZnO_{0.05}$ $V_2O_{5(0.90)}$]. The deconvolution of the V2p spectrum indicates a multi-splitting accompanied by the characteristic satellites, suggesting the existence of different oxidation states [23]. The O1s signal is sufficiently close to the V2p1/2 to affect the background underneath of the V2p signal, as shown in Figure 3. The deconvolution of the Zn2p spectrum displays a doublet of intense and sharp peaks at 1021.88 eV and 1044.99 eV, assigned to Zn2p3/2 and Zn2p1/2 of Zn-nanorods [24]. A broad, low-intensity peak at 1021.07 eV was attributed to Zn-nanoparticles. The deconvolution of the Ag3d spectrum exhibits a doublet at 367.43 eV and 373.43 eV, characteristics for Ag3d5/2 and Ag3d3/2, respectively, with BE = 6.0 eV, referring to the metallic Ag [25,26]. For the O1s, a slight asymmetry of 530.11 eV is attributed to the O^{-2} ion of the crystalline network. The broad, low-intensity peak at 531.6 eV was identified as O^{-} and assigned to subsurface oxygen ions with lower electron densities than O^{-2} [27].

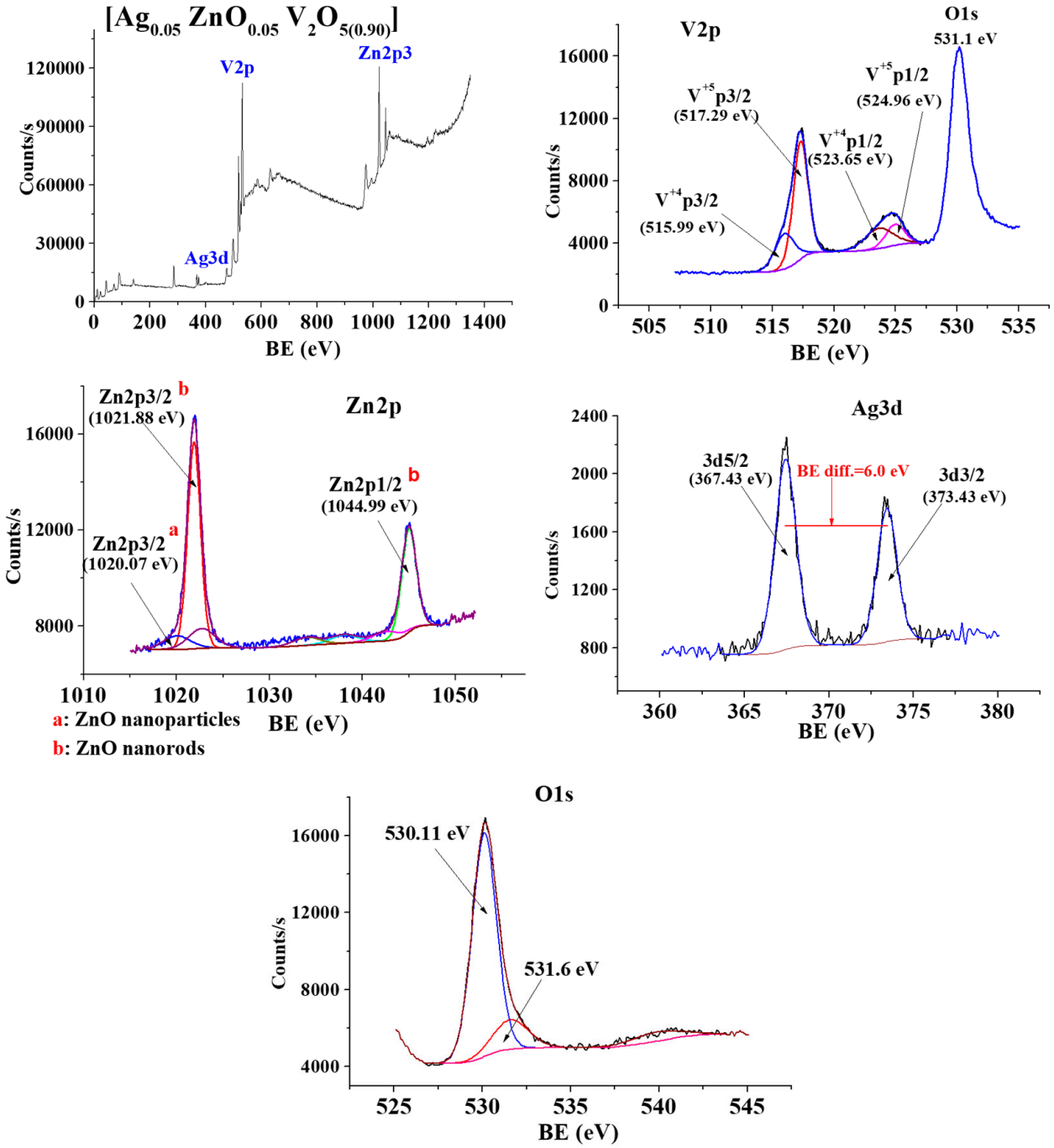

Figure 3. XP-spectra of [$Ag_{0.05}$ $ZnO_{0.05}$ $V_2O_{5(0.90)}$] and its constituent metallic species.

For [$Ag_{0.05}$ $ZnO_{0.05}$ $V_2O_{5(0.90)}$]$_N$, the spectra of V2p as dominant ionic species is not effected by the change in the electrostatic potential due to the doping with nitrogen, Figure 4. In addition, no chemical shift was observed for the binding energy of the Ag3d core level, confirming the Ag metallic state. The spectra of Zn2p show a chemical shift to higher binding energies of 0.26 eV and 0.17 eV for the main two peaks of Zn2p3/2 and Zn2p1/2, respectively. This most probably linked with the formation of Zn_3N_2 and/or the change in the electrostatic potential [27]. The spectra of N1s depicts a doublet at 399.48 eV and 400.4 eV, assigned to Zn_3N_2 and VN, respectively [28]. In comparison to O1s in [$Ag_{0.05}$ $ZnO_{0.05}$ $V_2O_{5(0.90)}$], the O1s spectra in [$Ag_{0.05}$ $ZnO_{0.05}$ $V_2O_{5(0.90)}$]$_N$ show a higher value in BE. This could be due to N-doping, which raises the concentration of O^- species [29].

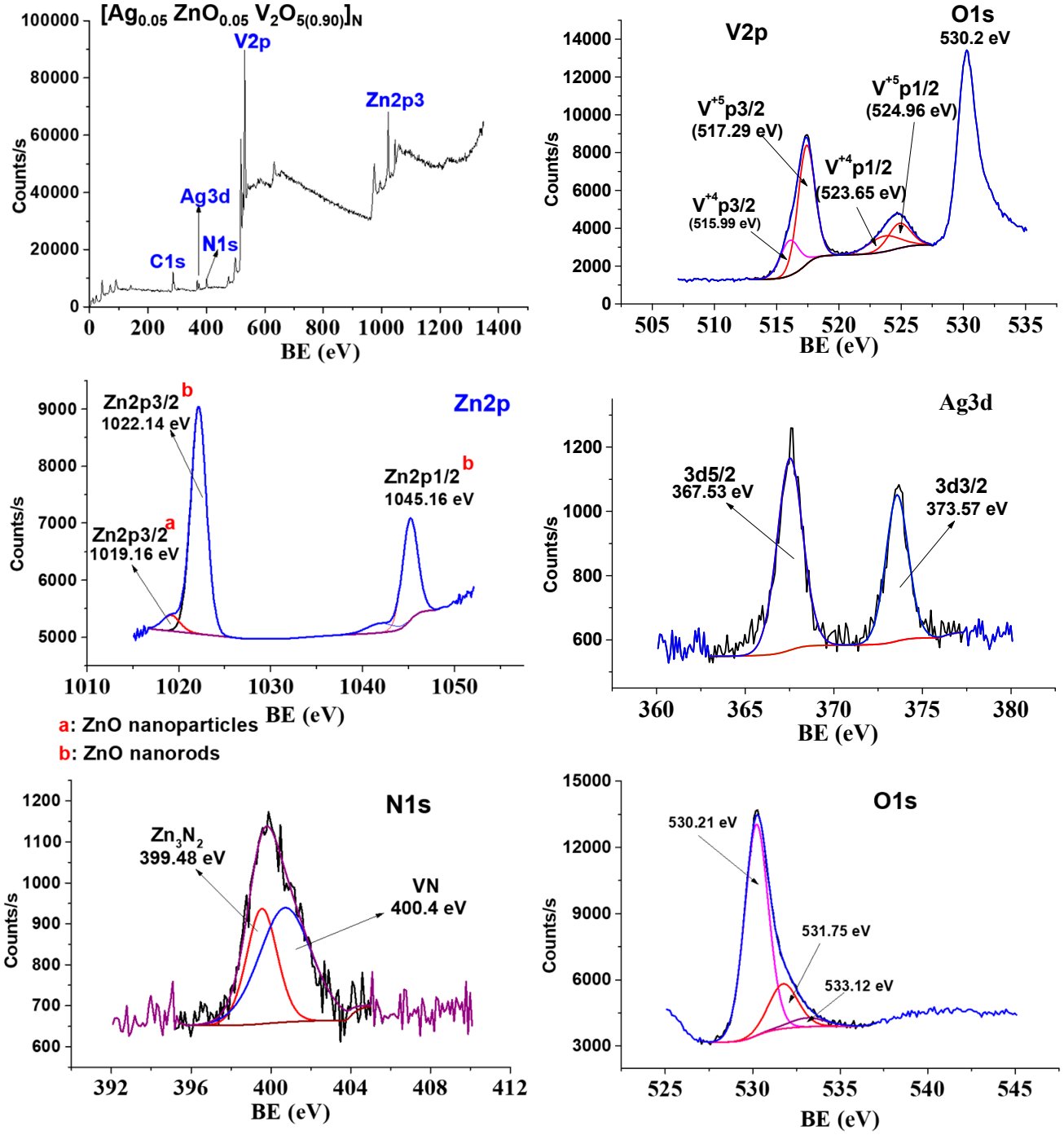

Figure 4. XP-spectra of $[Ag_{0.05}\ ZnO_{0.05}\ V_2O_{5(0.90)}]_N$ and its constituent metallic species.

SEM images of $[Ag_{0.05}\ ZnO_{0.05}\ V_2O_{5(0.90)}]$ and $[Ag_{0.05}\ ZnO_{0.05}\ V_2O_{5(0.90)}]_N$ are shown in Figure 5a,b. The lattice of $[Ag_{0.05}\ ZnO_{0.05}\ V_2O_{5(0.90)}]$ appears more ordered and homogenous as a tri-constitute composite than that of $[Ag_{0.05}\ ZnO_{0.05}\ V_2O_{5(0.90)}]_N$, indicating the destruction of the crystal system by N-doping (cf. Figure 2). In the SEM image of $[Ag_{0.05}\ ZnO_{0.05}\ V_2O_{5(0.90)}]$, nanofibers with lengths between 5 and 10 μm are dispersed in particles with a wide range of sizes between 0.5 and 5 μm. The SEM profile of $[Ag_{0.05}\ ZnO_{0.05}\ V_2O_{5(0.90)}]_N$ displays surface-large cavities ranging from 10 to 70 μm. The compatibility between VN and Zn_3N_2 is indicated and repels the metallic Ag onto the cavity's mouth.

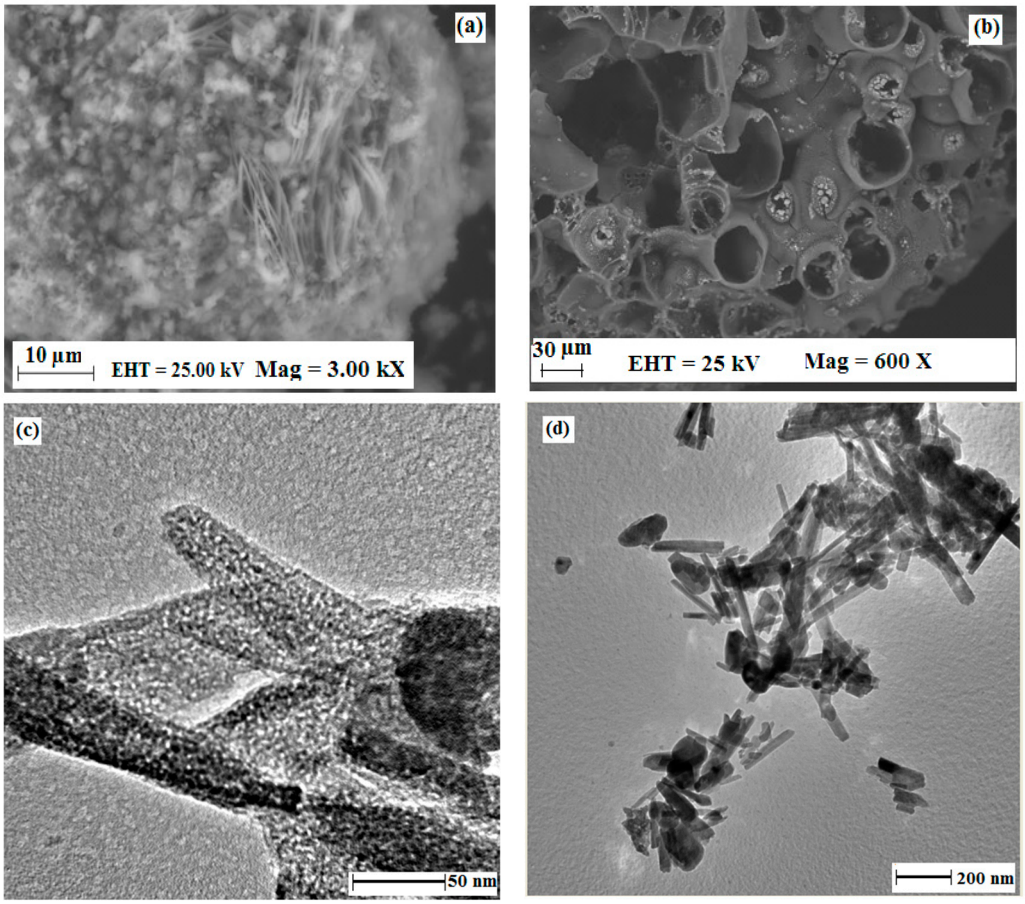

Figure 5. The SEM and TEM image. (**a**) SEM image of [$Ag_{0.05}$ $ZnO_{0.05}$ $V_2O_{5(0.90)}$], (**b**) SEM image of [$Ag_{0.05}$ $ZnO_{0.05}$ $V_2O_{5(0.90)}]_N$, (**c**) TEM image of [$Ag_{0.05}$ $ZnO_{0.05}$ $V_2O_{5(0.90)}$], and (**d**) TEM image of [$Ag_{0.05}$ $ZnO_{0.05}$ $V_2O_{5(0.90)}]_N$.

In the TEM image of [$Ag_{0.05}$ $ZnO_{0.05}$ $V_2O_{5(0.90)}$], Figure 5c, Ag nanoparticles with a size of ≈2–5 nm are sited on vanadia and $Zn_3(VO_4)_2$ nano-rods in a homogeneous distribution, whereas in the [$Ag_{0.05}$ $ZnO_{0.05}$ $V_2O_{5(0.90)}]_N$, Figure 5d, it is clear that the reconstruction of the tri-constitute composite is due to the formation of Zn_3N_2 and VN nano-rods with high compatibility and repelling Ag nanoparticles to aggregate onto the mouth of the pores (cf. SEM images, XPS and XRD).

The surface analysis estimated from adsorption–desorption isotherms is given in Table 1, including specific surface areas (S_{BET}, m^2/g), pore volumes (Vp, cc g^{-1}) calculated at 0.95 P^0/P, and the average pore diameter ($D_p{}^{CP}$) assuming a cylindrical pore (CP) model derived from the PSD curve, which are depicted in Figure 6. Table 1 shows that textural remodeling of [$Ag_{0.05}$ $ZnO_{0.05}$ $V_2O_{5(0.90)}$] with N-doping results in a significant increase in surface area and a decline in pore dimensions. From the XRD profiles, the N-doping collapses the crystal structure and creates a multimodal PSD curve with different populations, as shown in Figure 6. The PDS curves show a primary peak of the most frequent hydraulic radius at 3.8 nm and 2.9 nm for [$Ag_{0.05}$ $ZnO_{0.05}$ $V_2O_{5(0.90)}$] and [$Ag_{0.05}$ $ZnO_{0.05}$ $V_2O_{5(0.90)}]_N$, respectively. Nitrogen adsorption–desorption isotherms of the as-prepared composite catalysts are compared in Figure 6. There are considerable differences between these isotherms, although they all represent type II adsorption isotherm with type H3 hysteresis loops, characteristics of slit-like pore materials [30]. It is obvious that the hysteresis loop obtained for [$Ag_{0.05}$ $ZnO_{0.05}$ $V_2O_{5(0.90)}$] suggests the occurrence of capillary condensation and the existence of mesopores. After the N-doping, the hysteresis loop becomes narrower, possibly due to the reorganization of the pore system.

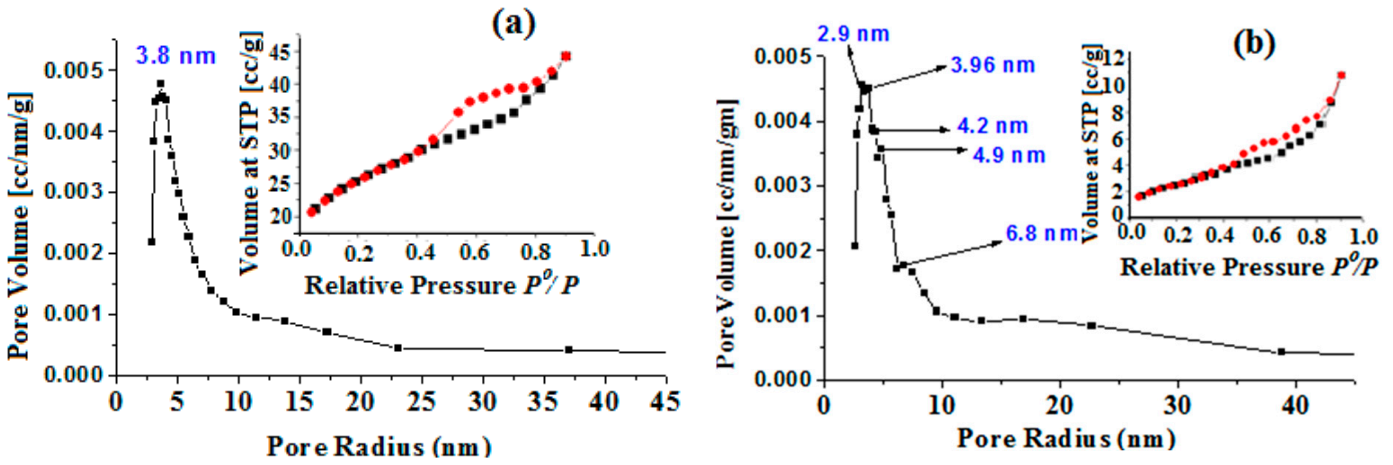

Figure 6. Isotherm and PSD curves of (**a**) [$Ag_{0.05}$ $ZnO_{0.05}$ $V_2O_{5(0.90)}$] and (**b**) [$Ag_{0.05}$ $ZnO_{0.05}$ $V_2O_{5(0.90)}$]$_N$.

Table 1. Textural analysis of the as-prepared photocatalysts.

Item	[$Ag_{0.05}$ $ZnO_{0.05}$ $V_2O_{5(0.90)}$]	[$Ag_{0.05}$ $ZnO_{0.05}$ $V_2O_{5(0.90)}$]$_N$
D_P^{CP} (nm)	7.22	6.71
$V_P^{0.95}$ (cm^3 g^{-1})	3.1	2.58
S_{BET} (m^2 g^{-1})	88.6	95.7

2.2. Optical Properties

The optical properties, viz., bandgap energy (E_g) and photoluminescence (PL) spectra, along with the textural analysis, determine the photocatalytic performance. A key strategy in optical property engineering is doping, which tunes a semiconductor's crucial structural, morphological, electrical, and optical properties that affect light absorption, redox potential, and charge carrier mobility. Figure 7 shows the Tauc plot and PL spectra for the as-prepared materials. The figure demonstrates that the two catalytic materials have E_g values in the visible region that are less than those of the bare V_2O_5 catalyst (2.2 eV) [31]. The two composite catalysts show more than one absorption peak. This can be attributable to any of the various transitions occurring between the energy levels induced by doping. In the metal-nonmetal doping, [$Ag_{0.05}$ $ZnO_{0.05}$ $V_2O_{5(0.90)}$]$_N$, many peaks are observed. This could be linked with the induction of new bands above the VB or below the CB due to the doping with a metal or a nonmetal, respectively; Figure 7 [32,33].

The PL spectra shed light on the types of oxygen vacancies and surface defects that affect optical properties. It is known that the noble metal Ag acts as an electron trap, which promotes the separation of photogenerated electrons and holes [17]. As shown in Figure 7, the two catalysts exhibit visible emission peaks centered at 581 nm related to the close band edge transition. Contrary to what is expected, the PL intensity of [$Ag_{0.05}$ $ZnO_{0.05}$ $V_2O_{5(0.90)}$]$_N$ is higher than that of [$Ag_{0.05}$ $ZnO_{0.05}$ $V_2O_{5(0.90)}$]. This is due to the quick recombination of photogenerated electron–hole pairs in the case of metal-nonmetal doping, whereas charge separation is effective in metal-doped V_2O_5 [34]. This could be attributed to the convergence of the energy levels created by metal-nonmetal co-doping, which facilitates the recombination of generated electron–hole pairs and/or the accumulation of Ag as plasmonic nanoparticles onto the cavities mouth, which diminishes the Ag role (cf. Figure 5).

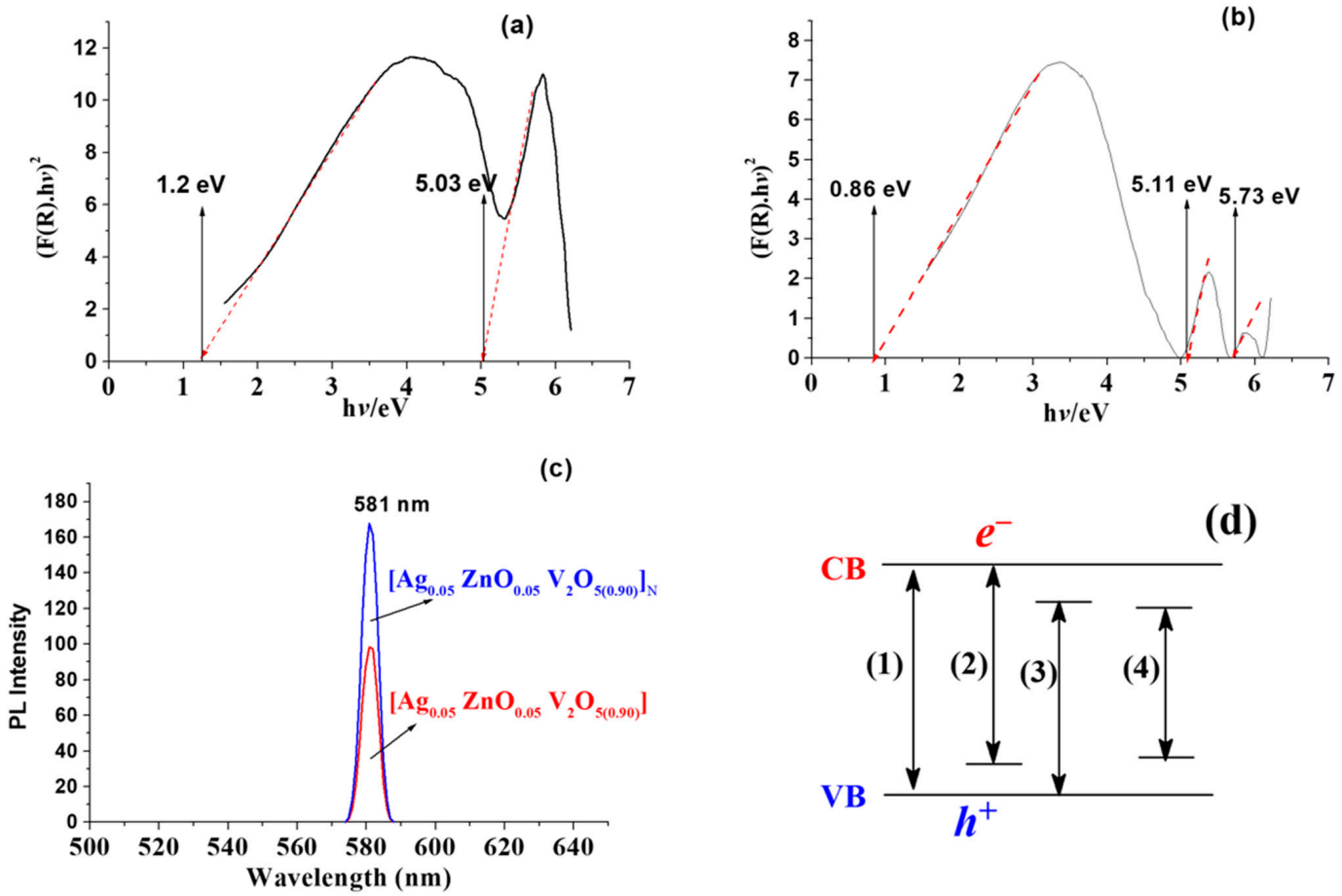

Figure 7. The bandgap energy calculated from Tauc plot of (**a**) $[Ag_{0.05}\ ZnO_{0.05}\ V_2O_{5(0.90)}]$, (**b**) $[Ag_{0.05}\ ZnO_{0.05}\ V_2O_{5(0.90)}]_N$; (**c**) the PL spectra of the as-prepared catalysts, and (**d**) the band structure of (1) bare catalyst, (2) metal-doped, (3) nonmetal-doped, and (4) metal-nonmetal-doped catalyst.

2.3. Catalytic Performance

The as-prepared materials are employed and assessed in the photodegradation of Congo red dye at ambient temperature after the textural analysis, surface chemistry, and optical properties are presented. In the case of macromolecule substrates, especially multiphase reactions, the mass transfer has a significant impact on the reaction kinetics and the catalytic performance as a whole [35]. The effect of mass transfer on the photocatalytic dye removal was investigated in the stirring range of 100–300 rpm at ambient temperature and the normal pH of the dye ~6.12, with a fixed catalyst dose of 0.5 g L^{-1}. To achieve the pre-equilibrium sorption of the substrate on the catalyst surface in each experiment, 100 mL of the dye solution with an initial concentration of 50 ppm was stirred at the selected stirring rate in a dark period for 1 h, followed by irradiation for 2 h. As shown in Figure 8, the degradation is increased by increasing the stirring rate from 100 to 200, showing a mass transfer-controlled regime over this part of the graph. It is worth noting that $[Ag_{0.05}\ ZnO_{0.05}\ V_2O_{5(0.90)}]_N$ is more affected by the stirring rate than $[Ag_{0.05}\ ZnO_{0.05}\ V_2O_{5(0.90)}]$. This could be attributed to the narrower pores of $[Ag_{0.05}\ ZnO_{0.05}\ V_2O_{5(0.90)}]_N$ which may not accommodate the bulky molecules of the dye, which leads to the occurrence of most of the reaction on the outer surface of the catalyst and diminishes the mass transfer effect. From the stirring rate of 200 to 300 rpm, it is clear that the dye degradation is independent of the stirring rate, revealing a kinetic-controlled regime.

All further experiments for investigation of the effect of the catalyst dose were conducted at a stirring rate of 200 rpm.

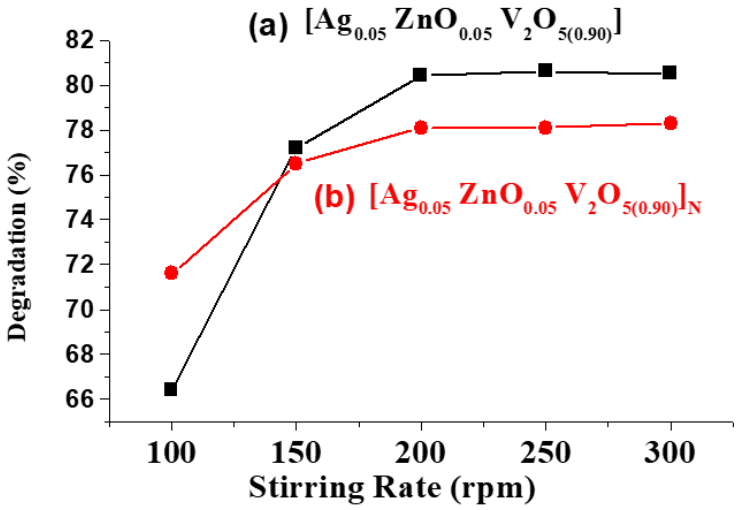

Figure 8. Effect of mass transfer on the photocatalytic degradation of Congo red dye.

The effect of the catalyst dose was investigated in the range of 0.5–1.5 g L^{-1}, irradiation period of 60–240 min and pH value of 6.12, as described in the experimental part, following the same procedures applied in the investigation of the effect of the mass transfer.

In the dark period, only the textural structure and the intensity of the active sites dictate the sorptivity of the catalytic material; the optical features have no impact on the removal of pollutants during this period [36]. As a result, throughout this time, as depicted in Figure 8, with the catalyst dose increasing from 0.5 to 1.5 g L^{-1}, the amount of the organic pollutant sorbed by the materials marginally increased. This is explained by the rise in active sites with increasing catalyst dosage. In general, $[Ag_{0.05}\ ZnO_{0.05}\ V_2O_{5(0.90)}]_N$ has the maximum sorptivity at various catalyst dosages. More specifically, in good agreement with the textural analysis, $[Ag_{0.05}\ ZnO_{0.05}\ V_2O_{5(0.90)}]_N$ at a catalyst dose of 1.5 g L^{-1} removed 55.6% of the organic pollutant, while $[Ag_{0.05}\ ZnO_{0.05}\ V_2O_{5(0.90)}]$ at the same concentration removed 52.4%.

During the irradiation period, the photocatalytic performance is governed by optical characteristics and textural structure. The low energy needs for producing e^-/h^* pairs and the inhibition of their radiative recombination process are shown by the low E_g and PL intensity, which improve photon efficiency. On the other hand, the increase in surface area and pore dimensions increases the availability of the catalyst's active sites and diminishes the diffusional limitation of reactants and products [37]. The two catalytic materials exhibit visible region absorption, with variations in E_g value, PL intensity, and surface analysis, as shown in Figure 7 and Table 1. Each of the three factors may have a different level of effect, but the difference in value of each of these factors determines which one is predominant. Even though $[Ag_{0.05}\ ZnO_{0.05}\ V_2O_{5(0.90)}]_N$ has a lower bandgap (0.86 eV) and a slightly higher surface area (95.7 $m^2\ g^{-1}$), it exhibits lower activity than $[Ag_{0.05}\ ZnO_{0.05}\ V_2O_{5(0.90)}]$, Figure 9. This reveals that the lower PL intensity, viz., more stable e^-/h^* pairs, and higher pore dimensions (diameter and volume) of $[Ag_{0.05}\ ZnO_{0.05}\ V_2O_{5(0.90)}]$ are the predominant factors. The Congo red macromolecule maximizes the role of pore dimensions by reducing reactant and product diffusional limitations.

Figure 9 depicts the effect of catalyst dose on catalytic performance. When the catalyst dose increased from 0.5 to 1 g L^{-1}, the catalytic rate of the utilized catalysts dramatically increased up to 120 min, where the degradation percentage reached 89.9% and 83.4% for $[Ag_{0.05}\ ZnO_{0.05}\ V_2O_{5(0.90)}]$ and $[Ag_{0.05}\ ZnO_{0.05}\ V_2O_{5(0.90)}]_N$, respectively. These percentages were not observed at 240 min of irradiation when the catalyst dose of 0.5 g L^{-1} was applied. A decrease in the degradation rate was seen over the last two hours, most probably due to the decrease in dye concentration, which decreases the probability of dye molecule active site collision. The two catalysts exhibited dampened activity with the increase in catalyst

dose to 1.5 g L^{-1}. This could be explained by the fact that the excess catalyst dose resists the penetration of light into the reaction medium [38].

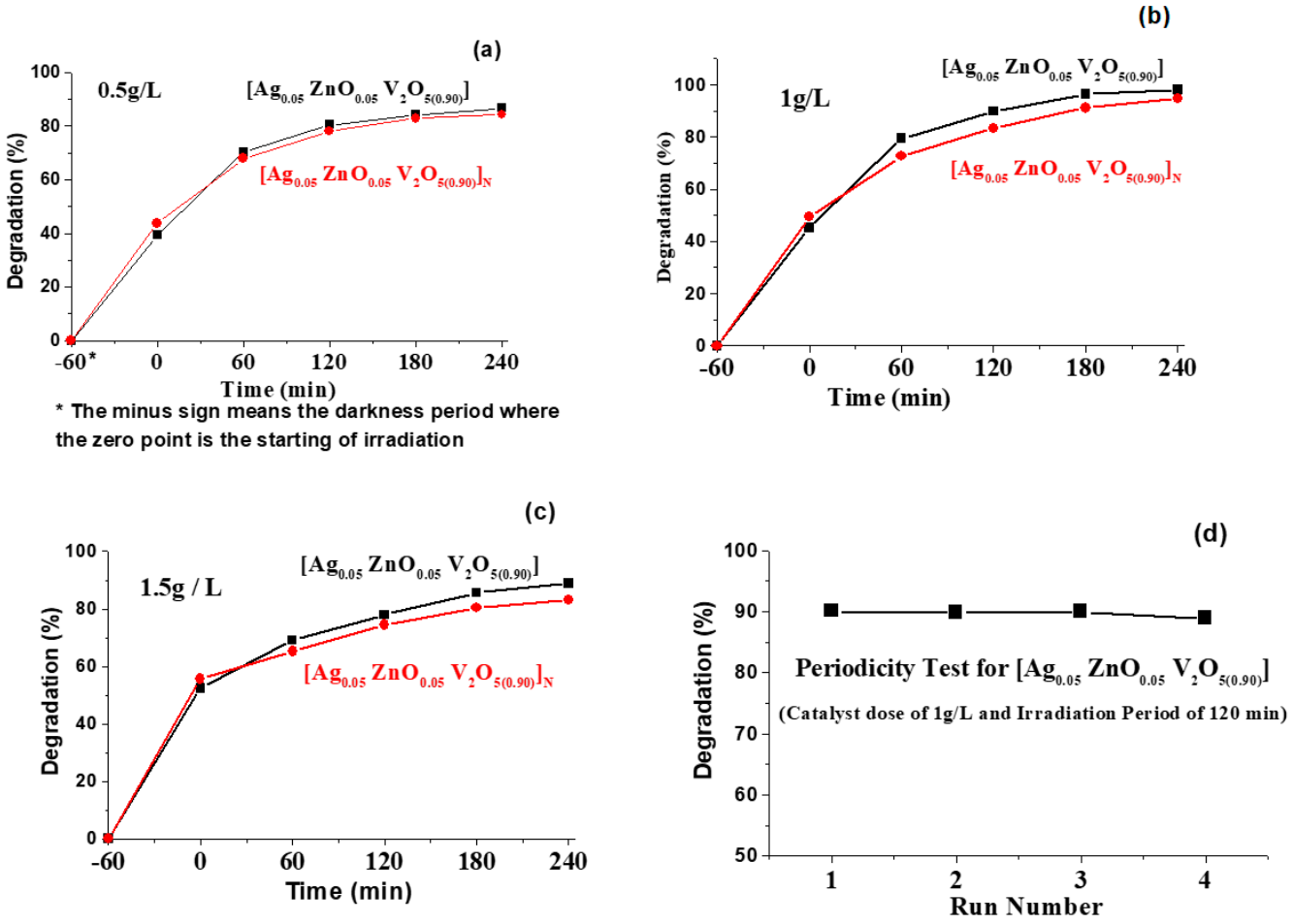

Figure 9. The catalytic performance of the as-prepared photocatalysts at catalyst dose of (**a**) 0.5 g L^{-1}, (**b**) 1.0 g L^{-1}, (**c**) 1.5 g L^{-1}, and (**d**) the reusability test for [$Ag_{0.05}$ $ZnO_{0.05}$ $V_2O_{5(0.90)}$].

Under the same experimental conditions, the uncatalyzed photodegradation of the Congo red dye was investigated to exhibit the employed catalysts' effect. After 4 h of irradiation, no significant changes were observed, referring to the catalyst's role in the photo-disposal of the dye.

2.4. The Effect of pH

The effect of pH value on the photocatalytic degradation of Congo red dye under visible light irradiation over [$Ag_{0.05}$ $ZnO_{0.05}$ $V_2O_{5(0.90)}$] was investigated at the previously detected optimum conditions, viz., a catalyst dose of 1g L^{-1}, stirring rate of 200 rpm and a period from 0 to 120 min. To attain the required pH, NaOH and HCl were used. Figure 10 depicts the behavior of photocatalytic efficiency with variations in pH value. In fact, in the acidic environment, two factors work against each other. The first promotes the catalytic activity by increasing the positive charges on the surface of the catalyst, which increases the electrostatic attraction between the active sites of the catalyst and the dye molecules [39]. The second, the photocatalytic system, is disrupted by the reaction of the catalyst components with the acid, which leads to a dramatic decrease in the catalytic activity [11]. It is noticeable that at a pH value of 2 or 3, the catalyst composition is rapidly affected by just placing it in the medium, whereas this is delayed in the case of pH = 5, where the decrease in catalytic activity starts after 90 min. In the alkaline medium, both factors act in one direction, which is to suppress the catalytic activity. The negatively charged [$Ag_{0.05}$

$ZnO_{0.05}$ $V_2O_{5(0.90)}$] surface and the negatively charged molecules of dye in the higher pH solution are subjected to columbic repulsion, which hinders the photocatalytic activity [39]. The reduced activity in alkaline medium, on the other hand, could be attributed to the catalyst components being converted to vanadate salt and/or AgOH and $Zn(OH)_2$, which remove them from their photocatalytic role. Although the catalytic activity at pH = 5 is higher than at pH = 7 at first (after 30 min), it starts to decrease after 60 min as the catalyst breaks down as a result of the acidic medium, as discussed before. Therefore, it seems that a pH of 6.12 is the most appropriate medium for [$Ag_{0.05}$ $ZnO_{0.05}$ $V_2O_{5(0.90)}$].

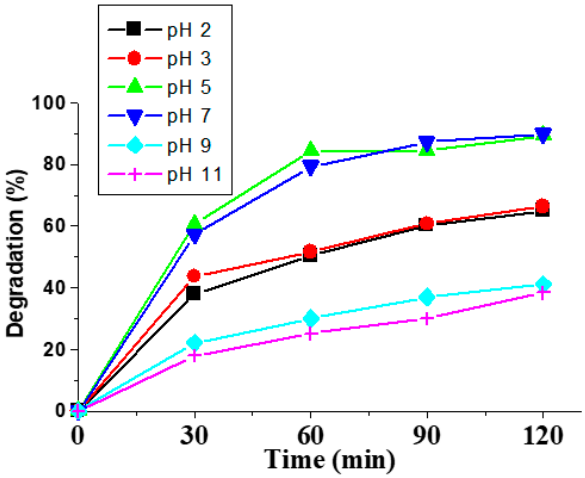

Figure 10. Effect of pH on photodegradation of Congo red dye over [$Ag_{0.05}$ $ZnO_{0.05}$ $V_2O_{5(0.90)}$].

2.5. Kinetics

The present reaction of photocatalytic degradation of Congo red dye by oxidation with O_2 can be described by the Eley–Rideal mechanism, which defines the reaction mechanism of an adsorbed reactant with another reactant in the gaseous phase [40]. The photocatalyst forms electron–hole pairs between its valence and conduction bands as a result of irradiation. In the presence of oxygen, a photo-excited electron forms a superoxide anion (O^{-2}) that, when protonated, produces an OH radical. The positive hole contributes to the breakdown of organic molecules by generating an OH radical when it reacts with water [41].

Eley–Rideal mechanism can be described by the following equation:

$$-\frac{dC}{dt} = K_r C\theta_{O_2,} \quad (1)$$

where K_r = reaction rate constant, C = concentration of the dye, and θ_{O_2} = concentration of adsorbed oxygen.

In the current batch process, the continuous aeration (at room temperature, 24 °C) makes the reaction independent of the oxygen surface concentration. Hence, Equation (1) devolves into Equation (2), which, upon integration, transforms into Equation (3), where K_{ap} is the apparent or observed rate constant and C_o is the initial concentration of the organic dye (50 ppm).

$$-\frac{dC}{dt} = K_{ap}C \quad (2)$$

$$ln\frac{C_o}{C} = K_{ap}t \quad (3)$$

Applying Equation (3) to the experimental data collected at a catalyst dosage of 1 g L^{-1} yields Figure 11. From Figure 10, the obtained apparent rate constants (regression coefficients) of the as-prepared photocatalyst are 0.99559 and 0.99814 for [$Ag_{0.05}$ $ZnO_{0.05}$ $V_2O_{5(0.90)}$] and [$Ag_{0.05}$ $ZnO_{0.05}$ $V_2O_{5(0.90)}$]$_N$, respectively. The slight increase in the rate constant of

$[Ag_{0.05}\ ZnO_{0.05}\ V_2O_{5(0.90)}]_N$ could be attributed to its narrower pores, which make the most reaction take place on the surface that facilitates mass transfer and reduces diffusional limitation, in good agreement with the findings observed from the investigation of the effect of mass transfer on reaction kinetics.

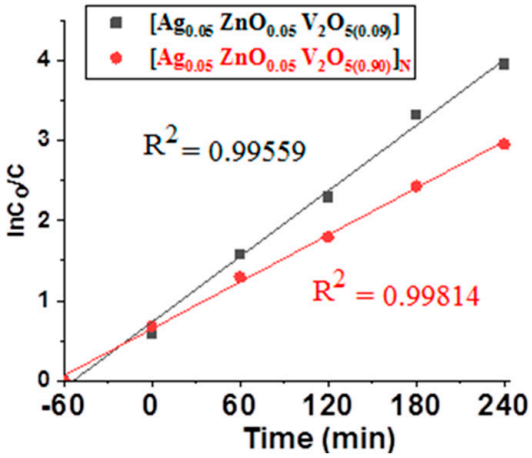

Figure 11. Kinetic expression for the employed photocatalysts at the catalyst dose of 1 g L^{-1}.

2.6. Photo-Degradation Mechanism

The enhanced visible light photocatalytic capabilities of the $[Ag_{0.05}\ ZnO_{0.05}\ V_2O_{5(0.90)}]$ composite catalyst were explained by the proposed processes in Figure 12. When a photocatalyst is exposed to light energy that is equal to or greater than the band gap energy (E_g), an excited electron in the valence band (VB) of the photocatalyst is promoted to the conduction band (CB), where it produces a positive hole (h^+) in the VB and an electron (e^-) in the CB, as shown in Equation (4):

$$[Ag_{0.05}\ ZnO_{0.05}\ V_2O_{5(0.90)}] + h\nu \rightarrow [Ag_{0.05}\ ZnO_{0.05}\ V_2O_{5(0.90)}](h^+{}_{VB} + e^-{}_{CB}) \quad (4)$$

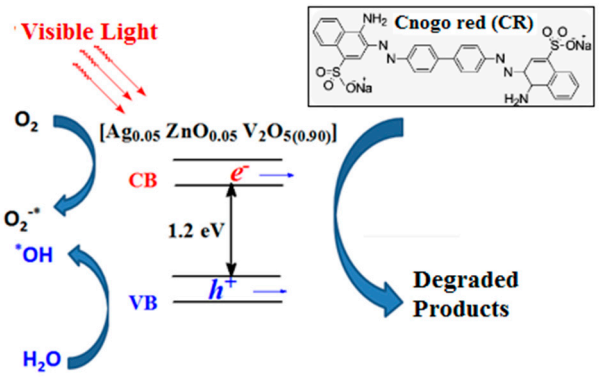

Figure 12. The proposed mechanism of CR degradation over $[Ag_{0.05}\ ZnO_{0.05}\ V_2O_{5(0.90)}]$ photocatalyst under visible-light irradiation.

The $h^+{}_{VB}$ and $e^-{}_{CB}$ pairs that were photogenerated were transported to the catalyst surface. On the catalyst surface, they interact with water, dissolve oxygen and surface hydroxyl groups (OH) to form highly potential hydroxyl and superoxide radical anions, as shown in Equations (5) and (6).

$$[Ag_{0.05}\ ZnO_{0.05}\ V_2O_{5(0.90)}](h^+{}_{VB}) + H_2O \text{ or } OH \rightarrow [Ag_{0.05}\ ZnO_{0.05}\ V_2O_{5(0.90)}] + H^+ + OH \quad (5)$$

$$[Ag_{0.05}\ ZnO_{0.05}\ V_2O_{5(0.90)}](e^-{}_{CB}) + O_2 \rightarrow [Ag_{0.05}\ ZnO_{0.05}\ V_2O_{5(0.90)}] + O_2{}^{\cdot -} \quad (6)$$

Then, the potential radicals were attacked, causing the dye to be degraded into a variety of chemical intermediates, which were then fully mineralized into carbon dioxide, water, ammonium, and nitrate ions [9,12,42,43], as in Equation (7).

$$\text{CR dye} + OH + O_2^- \rightarrow \text{intermediates} \rightarrow CO_2 + H_2O + NO^{-3} + NH^{+4} \quad (7)$$

The dye mineralization with time was confirmed by the determination of total organic carbon (TOC). It was obtained that the TOC was reduced after 4 h of irradiation in visible light by 85% and 74% in the cases of $[Ag_{0.05}\ ZnO_{0.05}\ V_2O_{5(0.90)}]$ and $[Ag_{0.05}\ ZnO_{0.05}\ V_2O_{5(0.90)}]_N$ photocatalysts at a dose of 1 g L^{-1}, respectively.

2.7. Periodicity Test

The most important factor in industrial applications is the catalyst's capacity to be used in several cycles. The $[Ag_{0.05}\ ZnO_{0.05}\ V_2O_{5(0.90)}]$ catalyst reusability test, as a promised catalyst, was conducted under the optimal conditions (catalyst dose of 1 g L^{-1} and irradiation time of 120 min), where any change in catalytic performance is obvious. Figure 9 depicts the catalyst stability throughout four subsequent cycles.

2.8. Catalyst Comparability

The catalyst's comparison to earlier catalysts is one of the criteria for evaluation. When comparing the catalytic performance of organic pollutants removal in photocatalysis, the catalyst type (cost and ease of preparation), reaction variables such as light source, reaction time, and yield of the desired product must all be considered. Table 2 provides a summary of the photocatalytic performance of various catalysts during the disposal of Congo red dye. $[Ag_{0.05}\ ZnO_{0.05}\ V_2O_{5(0.90)}]$, the catalyst under research, has a tolerable photodegradation rate in terms of the percentage of degradation, reaction time, and irradiation light compared to other catalysts described in the literature. Other advantages may be added to the previously mentioned catalyst as it was primarily made from solid waste materials.

Table 2. Comparison of the photocatalytic disposal of Congo red dye over various catalysts.

Catalyst	Light Source	Time (min)	%Degradation	References
Chitosan/nano-CdS	Xenon lamp (300 W)	180	85.9	[44]
TNA-450	UV-LED- 400 nm (0.6 W)	300	100	[45]
m-alginate/Fe_2O_3/CdS composite	xenon lamp (300 W)	300	91.6	[46]
TiO_2-SWNT-P-21	UV-A 350 nm (8 W)	80	82	[47]
Sulfanilic acid-modified P25 TiO_2	halogen-tungsten lamp 400 nm (300 W)	210	90	[48]
$[Ag_{0.05}\ ZnO_{0.05}\ V_2O_{5(0.90)}]$	300 W high-pressure mercury lamp	120	89.9	This work

3. Materials and Methods

3.1. Materials

The vanadia spent catalyst was gifted by the Suez Company for Fertilizers Production (SCFP) during the annual maintenance of the sulfuric acid production unit. Silver solution waste was collected from photography shops. The blast furnace dust used in this study as a zinc source was obtained from the EZZ Flat Steel Company in Ain Sokhna, Suez, Egypt, with the composition displayed in Table 3. All chemicals used in the extraction of the metallic species are of analytical grade and are used as received without further treatment.

Table 3. The elemental analysis of the utilized blast furnace dust.

Element	O	Zn	C	Fe	Si	Ca	Al	Mg	Pb	S
wt.(%)	35.1	5.13	28.9	25.2	1.72	1.33	1.28	0.32	0.50	0.44

3.2. Extraction of Metallic Species

3.2.1. Zn

Zinc, as the objective metal, was extracted from blast furnace slag using the economic and chemically optimized method reported by Aiyuan et al. [49]. NH_3–CH_3COONH_4–H_2O system was used as an alkaline lixiviant at a total ammonia concentration of 5 mol L^{-1}, ammonia: ammonium ratio of 1:1, and a solid: liquid ratio of 1:5 with a stirring speed of 300 r.p.m. at the ambient temperature (27 °C). The leaching solution was filtered, and the remaining residue was washed with demineralized water. The zinc concentration in the obtained filtrate was determined using EDTA volumetric analysis.

3.2.2. Ag

The whole silver in the solution waste was precipitated as silver sulfide using sodium sulfide as a precipitant reagent [50,51]. The obtained precipitate was washed thoroughly with demineralized water and then dried at 60 °C for 2 h under vacuum. The obtained precipitate was ground into powder and oxidized into Ag_2SO_4 using 50% HNO_3 at 70 °C where a light yellow precipitate was obtained. The precipitate was washed with cold demineralized water and vacuum dried for 2 h at 60 °C. At 70 °C, 5 g of Ag_2SO_4 was dissolved in 100 mL of demineralized water, and then 0.2 M sodium acetate was added to precipitate Ag as Ag-acetate, Equations (8)–(10):

$$2AgX + Na_2S \rightarrow Ag_2S + 2NaX, \qquad X = NO_3{}^- \text{ and/or } I^- \tag{8}$$

$$3Ag_2S + 8HNO_3\ (50\%) \xrightarrow[\text{Stirring}]{70\ ^\circ C} Ag_2SO_4\ (\text{light yellow}) + 8NO + 4H_2O \tag{9}$$

$$Ag_2SO_4 + CH_3COONa \rightarrow CH_3COOAg\ (\text{light grey}) + Na_2SO_4 \tag{10}$$

Finally, the obtained Ag-acetate was filtered, washed with demineralized water, dried at 60 °C for 2 h under vacuum and put in a brown glass bottle.

3.2.3. Extraction of V_2O

Based on the composition of the spent catalyst displayed in Table 4, procedures for extracting vanadium were developed. The sample was ground and roasted at 650 °C to volatile sulfur and concentrate the other constituents [52,53]. The roasted sample was ground again for leaching with NaOH. A 100 g of the roasted sample was mixed with 400 mL of 8 M NaOH and stirred at 100 °C for 2 h. The slurry was filtered to recover the sodium vanadate solution. Ammonium chloride solution was added to the sodium vanadate solution to precipitate ammonium metavanadate.

$$V_2O_5 + 2NaOH \rightarrow 2NaVO_3 + H_2O \tag{11}$$

$$NaVO_3 + NH_4Cl \rightarrow NH_4VO_3 + NaCl \tag{12}$$

The precipitate was recovered by filtration, washed three times with demineralized water, and then dried at 60 °C for 2 h under vacuum.

Table 4. Constituent analysis of the spent catalyst.

Item	V_2O_5	Fe_2O_3	SiO_2	S	Na_2O	K_2O	Al_2O
wt.(%)	5.2	0.82	44.6	38.2	2.24	7.6	1.22

3.3. Preparation of Composite Photocatalysts

3.3.1. Ag and ZnO Co-Doped V_2O_5

A calculated volume from the zinc leaching solution containing 0.4 zinc (0.5 ZnO) was drown and put in a 150 mL beaker. The precursors of vanadia (NH_4VO_3) and silver (CH_3COOAg) in the amounts of 11.6 g and 0.774 g, respectively, were added to the previous

zinc solution, and the slurry was agitated for 3 h at ambient temperature and for 2 h at 60 °C to obtain a homogenous paste. The paste was transferred to a silica–alumina crucible and put in a programmed muffle furnace with multistage heating. In the first stage, the furnace was programmed to heat at 110 °C for 2 h followed by the second stage, in which the temperature was raised with a ramp rate of 5 °C min^{-1} to reach 550 °C and hold for 2 h. The obtained hybrid catalytic material with the composition weight percent of 5% Ag, 5% ZnO, and 90% V_2O_5 was denoted as [$Ag_{0.05}$ $ZnO_{0.05}$ $V_2O_{5\ (0.90)}$].

3.3.2. Nitrogen Doped [$Ag_{0.05}$ $ZnO_{0.05}$ $V_2O_{5(0.90)}$]

The as-prepared hybrid material was doped with nitrogen using urea as a nitrogen source. The catalytic material was crushed with urea in a 1:4 (*w*/*w*) ratio, respectively [54]. The mixture was annealed for 1 h at 400 °C with a heating rate of 10 °C min^{-1} in an air atmosphere and then allowed to cool to room temperature. The nitrogen-doped composite catalyst was washed with demineralized water, dried at 70 °C, and crushed into a fine powder. The obtained catalytic material was denoted as [$Ag_{0.05}$ $ZnO_{0.05}$ $V_2O_{5(0.90)}$]$_N$.

3.4. Photocatalytic Performance

The photocatalytic degradation of Congo red dye was used as a probe to evaluate the catalytic activity of the as-prepared catalysts. A cylindrical batch-type quartz reactor was utilized for the photocatalytic performance test. The catalyst was maintained in suspension by magnetic stirring. In every experiment, aeration through bubbling with a small blower was used to make up for the water's dissolved oxygen. For visible light, a 300 W high-pressure mercury lamp was used (Yaming Company, Shanghai, China). The bulb was turned on and warmed up for 10 min before each run to guarantee a steady light output. The influence of catalyst dosage on catalytic performance was investigated in the range of 0.5–1.5 g L^{-1}. The selected catalyst dose was dispensed in 100 mL of the dye solution with an initial concentration of 50 ppm. During both the dark and visible light irradiation periods, aliquots (10 mL) of the sample were drawn every hour and filtered through a sintered glass filter with a 0.2 µm Millipore disc. Each run was repeated twice, and the average value of each datum point was recorded. The concentration of the dye was monitored using a Shimadzu 1603 spectrophotometer at λ_{max}, 500 nm. The mineralization of the dye was confirmed by the determination of total organic carbon (TOC) in the initial dye concentration and the degraded products using analytikjena Multi N/C 2100S, Jena, Germany. The efficiency of the catalytic photodegradation process was estimated using Equation (13):

$$Degradation\ (\%) = \frac{C_o - C_t}{C_o} \times 100 \quad (13)$$

where C_o is the dye initial concentration (50 ppm), C_t is the dye concentration at time "*t*".

3.5. Testing Procedures

The elemental analysis of the spent catalyst and the blast furnace dust was determined using XRF (Advanced Axios Model, Lelyweg, The Netherlands) analytical analysis, which involved pressing 10 g of the sample into an aluminium cup with 2 g of wax as a binder and then exposing the disc to X-rays. The FT-IR analyses of the as-prepared catalysts were obtained using Perkin Elmer FT-IR spectrometer, Waltham, MA, USA where the spectrum was recorded between 400 and 4000 cm^{-1}. Nitrogen adsorption–desorption isotherms at 196 °C were used to characterize the textural analysis of the as-prepared hybrid catalytic systems utilizing the NOVA 3200 apparatus, Quantachrome, Boynton Beach, FL, USA. The samples were heated at 160 °C for 2 h under vacuum (104 Torr) for surface degassing. The surface areas (S_{BET}) were calculated using the BET equation from the adsorption isotherms branch. The Barrett, Joyner, and Halenda (BJH) approach was used to compute the pore size distribution from the isotherm desorption branch. An X-ray diffract-meter, PANalytical Model X'Pert PRO (Malvern Panalytical Ltd., Malvern, UK) with a Cu K radiation (k = 1.5418 A°) and a scanning rate of 0.3 min^{-1} was used for the XRD analysis.

For surface composition, the X-ray photoelectron spectroscopy (XPS) data were collected on K-ALPHA (Thermo Fisher Scientific, Waltham, MA, USA) using monochromatic X-ray Al K-alpha radiation with a spot size of 400 micro m at a pressure of 10–9 mbar and a full-spectrum pass energy of 200 eV and a narrow-spectrum pass energy of 50 eV. The diffusional reflectance and photoluminance spectra were recorded to study the optical characterization. The SEM images were examined on a Zeiss Evo 10 tungsten filament-based scanning electron microscope. The diffusional reflectance spectra were acquired using a Jasco V-750 spectrophotometer, Heckmondwike, UK, in the wavelength range of 200–800 nm. A spectrofluorometer (JASCO FP-6500, Tokyo, Japan) with an excitation wavelength of 300 nm was used to record the photoluminance (PL) characteristics of the samples at room temperature.

4. Conclusions

Hybrid photocatalysts were successfully and completely prepared from worthless waste materials. The use of the organometallic and ammonium salt of the extracted metals as auto-templated precursors enhanced the compatibility between the different constituents for the preparation of mesoporous catalytic material. Doping with metals and metal-nonmetals significantly reduces E_g. The degree of dispersion of Ag particles has a significant impact on the PL spectra and, consequently, the photocatalytic performance. The PL-spectra along with the pore dimensions exhibit the predominance in the photocatalytic activity in the degradation of macromolecules of Congo red dye. The as-prepared catalysts' catalytic performance is consistent with their optical and textural properties. The SEM and TEM images illustrated the formation of homogenous dispersion of Ag nanoparticles on vanadia and $Zn_3(VO_4)_2$ nano-rods with regular lattice in the case of [$Ag_{0.05}$ $ZnO_{0.05}$ $V_2O_{5(0.90)}$], which collapsed and reorganized with N-doping due to the formation of Zn_3N_2 and VN nano-rods. The composite catalyst [$Ag_{0.05}$ $ZnO_{0.05}$ $V_2O_{5(0.90)}$] with low PL intensity exhibited higher activity and reached 98.1% disposal of the organic pollutant after 240 min and a catalyst dose of 1 g L^{-1}. The pH effect on the catalytic performance exhibited the breakdown of the catalytic system in the acidic medium, whereas in the alkaline medium, the electric repulsion between negative charges on the catalyst surface and the negatively charged dye molecules caused a dampening of activity. Comparing the current catalyst with the catalysts described in the literature, it exhibited a reasonable photodegradation rate. The kinetic investigation depicted that the Congo red dye macromolecules maximized the role of pore dimensions. The periodicity test illustrated the stability of [$Ag_{0.05}$ $ZnO_{0.05}$ $V_2O_{5(0.90)}$] through four successive cycles.

Author Contributions: Conceptualization and writing—original draft preparation, N.H.S.; methodology, S.R.A.-M.; validation and visualization, A.H.R.; formal analysis, H.A.E.; investigation, E.A.A.-S.; resources, N.M.A.-T. All authors have read and agreed to the published version of the manuscript.

Funding: This work was supported by King Khalid University's Deanship of Scientific Research (grant no. R. G. P 2/38/44).

Data Availability Statement: The data are contained within the article.

Conflicts of Interest: The authors declare no conflict of interest.

References

1. Chen, C.; Ma, W.; Zhao, J. Semiconductor-mediated photodegradation of pollutants under visible-light irradiation. *Chem. Soc. Rev.* **2010**, *39*, 4206–4219. [CrossRef]
2. Zamani, A.; Sadjadi, M.S.; Mahjoub, A.; Yousefi, M.; Farhadyar, N. Synthesis, characterization and investigation of photocatalytic activity of $ZnMnO_3/Fe_3O_4$ nanocomposite for degradation of dye Congo red under visible light irradiation. *Int. J. Ind. Chem.* **2020**, *11*, 205–216. [CrossRef]
3. Thomas, M.; Naikoo, G.A.; Sheikh, M.U.-D.; Bano, M.; Khan, F. Effective photocatalytic degradation of Congo red dye using alginate/carboxymethyl cellulose/TiO_2 nanocomposite hydrogel under direct sunlight irradiation. *J. Photochem. Photobiol. A* **2016**, *327*, 33–43. [CrossRef]

4. Saeed, M.; Muneer, M.; Mumtaz, N.; Siddique, M.; Akram, N.; Hamayun, M. Ag-Co_3O_4: Synthesis, characterization and evaluation of its photocatalytic activity towards degradation of rhodamine B dye in aqueous medium. *Chin. J. Chem. Eng.* **2018**, *26*, 1264–1269. [CrossRef]
5. Lachheb, H.; Puzenat, E.; Houas, A.; Ksibi, M.; Elaloui, E.; Guillard, C.; Herrmann, J.-M. Photocatalytic degradation of various types of dyes (Alizarin S, Crocein Orange G, Methyl Red, Congo Red, Methylene Blue) in water by UV-irradiated titania. *Appl. Catal. B* **2002**, *39*, 75–90. [CrossRef]
6. Srivind, J.; Nagarethinam, V.S.; Suganya, M.; Balamurugan, S.; Prabha, D.; Balu, A.R. Visible light irradiated photocatalytic performance of SnS_2-CdO nanocomposite against the degradation of rhodamine B (cationic) and congo red (anionic) dyes. *Mater. Sci. Eng. B* **2020**, *255*, 114530. [CrossRef]
7. Sathiyavimal, S.; Vasantharaj, S.; Shanmugavel, M.E.; Manikandan, E.; Nguyen-Trie, P.; Brindhadevi, K.; Pugazhendhi, A. Facile synthesis and characterization of hydroxyapatite from fish bones: Photocatalytic degradation of industrial dyes (crystal violet and Congo red). *Prog. Org. Coat.* **2020**, *148*, 10589. [CrossRef]
8. Saeed, M.; Siddique, M.; Usman, M.; ul Haq, A.; Khan, S.G.; Abdur Raoof, H. Synthesis and Characterization of Zinc Oxide and Evaluation of its Catalytic Activities for Oxidative Degradation of Rhodamine B Dye in Aqueous Medium. *Z. Phys. Chem.* **2017**, *231*, 1559–1572. [CrossRef]
9. Chin, Y.-H.; Sin, J.-C.; Lam, S.-M.; Zeng, H.; Lin, H.; Li, H.; Huang, L.; Mohamed, A.R. 3-D/3-Z-Scheme Heterojunction Composite Formed by Marimo-like Bi_2WO_6 an Mammillaria-like ZnO for Expeditious Sunligh Photodegradation of Dimethyl Phthalate. *Catalysts* **2022**, *12*, 1427. [CrossRef]
10. Byrne, C.; Subramanian, G.; Pillai, S.C. Recent advances in photocatalysis for environmental applications. *J. Environ. Chem. Eng.* **2018**, *6*, 3531–3555. [CrossRef]
11. Jamshaid, M.; Nazir, M.A.; Najam, T.; Shah, S.S.A.; Khan, H.M.; Rehman, A. Facile synthesis of Yb^{3+}-Zn^{2+} substituted M type hexaferrites: Structural, electric and photocatalytic properties under visible light for methylene blue removal. *Chem. Phys. Lett.* **2022**, *805*, 139939. [CrossRef]
12. Lam, S.-M.; Jaffari, Z.H.; Sin, J.-C.; Zeng, H.; Lin, H.; Li, H.; Mohamed, A.R.; Ng, D.-Q. Surface decorated coral-like magnetic $BiFeO_3$ with Au nanoparticles for effective sunlight photodegradation of 2,4-D and *E. coli* inactivation. *J. Mol. Liq.* **2021**, *326*, 115372. [CrossRef]
13. Shahzad, K.; Hussain, S.; Nazir, M.A.; Jamshaid, M.; Rehman, A.; Alkorbi, A.S.; Alsaiari, R.; Alhemiary, N.A. Versatile Ag_2O and ZnO nanomaterials fabricated via annealed Ag-PMOS and ZnO-PMOS: An efficient photocatalysis tool for azo dyes. *J. Mol. Liq.* **2022**, *356*, 119036. [CrossRef]
14. Nazir, M.A.; Najam, T.; Jabeen, S.; Wattoo, M.A.; Bashir, M.S.; Shah, S.S.A.; Rehman, A. Facile synthesis of Tri-metallic layered double hydroxides (NiZnAl-LDHs): Adsorption of Rhodamine-B and methyl orange from water. *Inorg. Chem. Commun.* **2022**, *145*, 11000. [CrossRef]
15. Venkatesham, N.; Reddy, K.R.; Rajanna, K.C.; Veerasomaiah, P. Vanadium Pentoxide as a Catalyst for Regioselective Nitration of Organic Compounds under Conventional and Nonconventional Conditions. *Synth. React. Inorg. Met.-Org. Nano-Met. Chem.* **2014**, *44*, 921–926. [CrossRef]
16. Kumawat, A.K.; Nathawat, R.; Rathore, S.; Mukhopadhyay, A.K. Band gap tuning possibilities in vanadium oxide. *Mater. Today Proc.* **2021**, *43*, 2939–2943. [CrossRef]
17. Varma, R.S.; Thorat, N.; Fernandes, R.; Kothari, D.C.; Patel, N.; Miotello, A. Dependence of photocatalysis on charge carrier separation in Ag-doped and decorated TiO_2 nanocomposites. *Catal. Sci. Technol.* **2016**, *6*, 8428–8440. [CrossRef]
18. Aziz, S.B.; Hussein, G.; Brza, M.A.; Mohammed, S.J.; Abdulwahid, R.T.; Saeed, S.R.; Hassanzadeh, A. Fabrication of Interconnected Plasmonic Spherical Silver Nanoparticles with Enhanced Localized Surface Plasmon Resonance (LSPR) Peaks Using Quince Leaf Extract Solution. *Nanomaterials* **2019**, *9*, 1557. [CrossRef]
19. AlShibane, I.; Hargreaves, J.S.J.; Hector, A.L.; Levasonb, W.; McFarlanea, A. Synthesis and methane cracking activity of a silicon nitride supported vanadium nitride nanoparticle composite. *Dalton Trans.* **2017**, *46*, 8782–8787. [CrossRef]
20. Jayarambabu, N.; Kumari, B.S.; Rao, K.V.; Prabhu, Y.T. Germination and Growth Characteristics of Mungbean Seeds (*Vigna radiata* L.) affected by Synthesized Zinc Oxide Nanoparticles. *Int. J. Curr. Eng. Technol.* **2014**, *4*, 3411–3416.
21. Rupa, A.V.; Manikandan, D.; Divakar, D.; Sivakumar, T. Effect of deposition of Ag on TiO2 nanoparticles on the photodegradation of Reactive Yellow-17. *J. Hazard. Mater.* **2007**, *147*, 906–913. [CrossRef] [PubMed]
22. Behnajady, M.A.; Modirshahla, N.; Shokri, M.; Rad, B. Enhancement of photocatalytic activity of TiO_2 nanoparticles by silver doping: Photodeposition versus liquid impregnation methods. *Glob. Nest. J.* **2008**, *10*, 1–7. [CrossRef]
23. Silversmit, G.; Depla, D.; Poelman, H.; Marin, G.B.; De Gryse, R. Determination of the V2p XPS binding energies for different vanadium oxidation states (V^{5+} to V^{0+}). *J. Electron Spectrosc. Relat. Phenom.* **2004**, *135*, 167–175. [CrossRef]
24. Yu, Z.-T.; Xu, J.-J.; Jiang, Y.-S.; Shi, Z.; Guo, Y.; Wang, D.J.; Chen, J.-S. Photoluminescent and photovoltaic properties observed in a zinc borate $Zn_2(OH)BO_3$. *J. Mater. Chem.* **2003**, *13*, 2227–2233. [CrossRef]
25. Gao, X.-Y.; Wang, S.-Y.; Li, J.; Zheng, Y.-X.; Zhang, R.-J.; Zhou, P.; Yang, Y.M.; Chen, L.-Y. Study of structure and optical properties of silver oxide films by ellipsometry, XRD and XPS methods. *Thin Solid Films* **2004**, *455*, 438–442. [CrossRef]
26. Masetti, E.; Bulir, J.; Gagliardi, S.; Janicki, V.; Krasilnikova, A.; Di Santo, G.; Coluzza, C. Ellipsometric and XPS analysis of the interface between silver and SiO_2, TiO_2 and SiN_x thin films. *Thin Solid Films* **2004**, *455*, 468–472. [CrossRef]

27. Shalaby, N.H.; Sayed, M.A. Stover ash—Extracted mixed oxides surface-doped with Ni for photo-degradation of water organic pollutants. *Int. J. Environ. Anal. Chem.* **2021**. [CrossRef]
28. Zhuk, S.; Siol, S. Chemical state analysis of reactively sputtered zinc vanadium nitride: The Auger parameter as a tool in materials design. *Appl. Surf. Sci.* **2022**, *601*, 154172. [CrossRef]
29. Wua, Q.-H.; Thissena, A.; Jaegermanna, W.; Liu, M. Photoelectron spectroscopy study of oxygen vacancy on vanadium oxides surface. *Appl. Surf. Sci.* **2004**, *236*, 473–478. [CrossRef]
30. Hu, Q.H.; Qiao, S.Z.; Haghseresht, F.; Wilson, M.A.; Lu, G.Q. Adsorption Study for Removal of Basic Red Dye Using Bentonite. *Ind. Eng. Chem. Res.* **2006**, *45*, 733–738. [CrossRef]
31. Srilakshmi, P.; Maheswari, A.U.; Sajeev, V.; Sivakumar, M. Tuning the optical bandgap of V_2O_5 nanoparticles by doping transition metal ions. *Mater. Today Proc.* **2019**, *18*, 1375–1379. [CrossRef]
32. Nah, Y.-C.; Paramasivam, I.; Schmuki, P. Doped TiO_2 and TiO_2 Nanotubes: Synthesis and Applications. *Chem. Phys. Chem.* **2010**, *11*, 2698–2713. [CrossRef]
33. Zaleska, A. Doped-TiO_2: A Review. *Recent Pat. Eng.* **2008**, *2*, 157–164. [CrossRef]
34. Maeda, M.; Yamada, T. Photocatalytic activity of metal-doped titanium oxide films prepared by sol-gel process. *J. Phys. Conf. Ser.* **2007**, *61*, 755–759. [CrossRef]
35. Makwana, V.D.; Son, Y.-C.; Howell, A.R.; Suib, S.L. The Role of Lattice Oxygen in Selective Benzyl Alcohol Oxidation Using OMS-2 Catalyst: A Kinetic and Isotope-Labeling Study. *J. Catal.* **2002**, *210*, 46–52. [CrossRef]
36. Shalaby, N.H. Photocatalytic Performance of Organically Templated Cr-Doped Co_3O_4 in Remediation of Industrial Wastewater: Effect of Order–Disorde in the Lattice. *Arab. J. Sci. Eng.* **2022**. [CrossRef]
37. Hansheng, L.; Jungang, W.; Congbiao, C.; Litao, J.; Bo, H.; Debao, L. Effects of macropores on reducing internal diffusion limitations in Fischer–Tropsch synthesis using a hierarchical cobalt catalyst Catalyst. *RSC Adv.* **2017**, *7*, 9436–9445. [CrossRef]
38. Emam, E.A.; Aboul-Gheit, N.A.K. Photocatalytic degradation of oil-emulsion in water/seawater using titanium dioxide. *Energy Sources A Recov. Util. Environ. Eff.* **2014**, *36*, 1123–1133. [CrossRef]
39. Sowmya, S.R.; Madhu, G.M.; Hashir, M. Studies on Nano-Engineered TiO_2 Photo Catalyst for Effective Degradation of Dye. *Mater. Sci. Eng.* **2018**, *310*, 012026. [CrossRef]
40. Huancong, S.; Min, H.; Yuandong, H.; Lifeng, C.; Linna, Z.; Mingqi, C.; Linhua, J.; Hussameldin, I.; Paitoon, T. Eley–Rideal model of heterogeneous catalytic carbamate formation based on CO_2-MEA absorptions with CaCO. *R. Soc. Open Sci.* **2019**, *6*, 1903. [CrossRef]
41. Palominos, R.; Freer, J.; Mondaca, M.A.; Mansilla, H.D. Evidence for hole participation during the photocatalytic oxidation of the antibiotic flumequine. *J. Photochem. Photobiol. A* **2008**, *193*, 139–145. [CrossRef]
42. Erdemoğlu, S.; Aksu, S.K.; Sayılkan, F.; İzgi, B.; Asiltürk, M.; Sayılkan, H.; Frimmel, F.; Güçer, S. Photocatalytic degradation of Congo Red by hydrothermally synthesized nanocrystalline TiO_2 and identification of degradation products by LC–MS. *J. Hazard. Mater.* **2008**, *155*, 469–476. [CrossRef]
43. Sin, J.-C.; Lam, S.-M.; Zeng, H.; Lin, H.; Li, H.; Huang, L.; Tham, K.-O.; Mohamed, A.R.; Lim, J.-W. Enhanced synchronous photocatalytic 4 chlorophenol degradation and Cr(VI) reduction by novel magnetic separable visible-light-driven Z-scheme $CoFe_2O_4$/P-doped BiOBr heterojunction nanocomposites. *Environ. Res.* **2022**, *212*, 113394. [CrossRef] [PubMed]
44. Zhu, H.; Jiang, R.; Xiao, L.; Chang, Y.; Guan, Y.; Li, X.; Zeng, G. Photocatalytic decolorization and degradation of Congo Red on innovative crosslinked chitosan/nano-CdS composite catalyst under visible light irradiation. *J. Hazard. Mater.* **2009**, *169*, 933–940. [CrossRef] [PubMed]
45. Natarajan, T.S.; Natarajan, K.; Bajaj, H.C.; Tayade, R.J. Energy Efficient UV-LED Source and TiO_2 Nanotube Array-Based Reactor for Photocatalytic Application. *Ind. Eng. Chem. Res.* **2011**, *50*, 7753–7762. [CrossRef]
46. Jiang, R.; Yao, J.; Zhu, H.; Fu, Y.; Guan, Y.; Xiao, L.; Zeng, G. Effective decolorization of congo red in aqueous solution by adsorption and photocatalysis using novel magnetic alginate/γ-Fe_2O_3/CdS nanocomposite. *Desalin. Water Treat.* **2014**, *52*, 238–247. [CrossRef]
47. Jafry, H.R.; Liga, M.V.; Barron, A.R. Single walled carbon nanotubes (SWNTs) as templates for the growth of TiO_2: The effect of silicon in coverage and the positive and negative synergies for the photocatalytic degradation of Congo red dye. *New J. Chem.* **2011**, *35*, 400–406. [CrossRef]
48. Guo, H.; Lin, K.; Zheng, Z.; Xiao, F.; Li, S. Sulfanilic Acid-Modified P25 TiO_2 Nanoparticles with Improved Photocatalytic Degradation on Congo Red under Visible Light. *Dyes Pigm.* **2012**, *92*, 1278–1284. [CrossRef]
49. Ma, A.; Zhang, L.; Peng, J.; Zheng, X.; Li, S.; Yang, K.; Chen, W. Extraction of zinc from blast furnace dust in ammonia leaching system. *Green Process. Synth.* **2016**, *5*, 23–30. [CrossRef]
50. Ganesan, R.; Narasimhalu, P.; Joseph, A.I.J.; Pugazhendhi, A. Synthesis of silver nanoparticle from X-ray film and its application in production of biofuel from jatropha oil. *Int. J. Energy Res.* **2020**, *45*, 17378–17388. [CrossRef]
51. Holloway, P.; Merriam, K.; Etsell, T. Nitric acid leaching of silver sulphide precipitates. *Hydrometallurgy* **2004**, *74*, 213–220. [CrossRef]
52. Mohanty, J.; Rath, P.C.; Bhattacharya, I.N.; Paramguru, R.K. The recovery of vanadium from spent catalyst: A case study. *Trans. Inst. Min. Metall. C* **2011**, *120*, 56–60. [CrossRef]

53. Pan, Y.X.; Sun, Y.; Qi, M.; Qin, R.; Che, X.; Zhang, Y. A clean and efficient method for separation of vanadium and molybdenum by aqueous two-phase systems. *J. Mol. Liq.* **2020**, *313*, 113540. [CrossRef]
54. Rengifo-Herrera, J.A.; Pulgarin, C. Photocatalytic activity of N, S co-doped and N-doped commercial anatase TiO_2 powders towards phenol oxidation and *E. coli* inactivation under simulated solar light irradiation. *J. Sol. Energy* **2010**, *84*, 37–43. [CrossRef]

Disclaimer/Publisher's Note: The statements, opinions and data contained in all publications are solely those of the individual author(s) and contributor(s) and not of MDPI and/or the editor(s). MDPI and/or the editor(s) disclaim responsibility for any injury to people or property resulting from any ideas, methods, instructions or products referred to in the content.